Front. Chem. Sci. Eng. 2023, 17(8): 1038−1050
https://doi.org/10.1007/s11705-022-2279-3

RESEARCH ARTICLE

Encapsulation of polyethylene glycol in cellulose-based porous capsules for latent heat storage and light-to-thermal conversion

Jiangwei Li, Lina Meng, Jiaxuan Chen, Xu Chen, Yonggui Wang (✉), Zefang Xiao, Haigang Wang, Daxin Liang, Yanjun Xie (✉)

Key Laboratory of Bio-based Material Science and Technology (Ministry of Education), College of Material Science and Engineering, Northeast Forestry University, Harbin 150040, China

Abstract Phase change materials are potential candidates for the application of latent heat storage. Herein, we fabricated porous capsules as shape-stable materials from cellulose-based polyelectrolyte complex, which were first prepared using cellulose 6-(*N*-pyridinium)hexanoyl ester as the cationic polyelectrolyte and carboxymethyl cellulose as the anionic polyelectrolyte to encapsulate polyethylene glycol by the vacuum impregnation method. Furthermore, the multi-walled carbon nanotube or graphene oxide, which were separately composited into the polyelectrolytes complex capsules to enhance thermal conductivity and light-to-thermal conversion efficiency. These capsules owned a typical core–shell structure, with an extremely high polyethylene glycol loading up to 34.33 $g \cdot g^{-1}$. After loading of polyethylene glycol, the resulted cellulose-based composite phase change materials exhibited high thermal energy storage ability with the latent heat up to 142.2 $J \cdot g^{-1}$, which was 98.5% of pure polyethylene glycol. Further results showed that the composite phase change materials demonstrated good form-stable property and thermal stability. Moreover, studies involving light-to-thermal conversion determined that composite phase change materials exhibited outstanding light-to-thermal conversion performance. Considering their exceptional comprehensive features, innovative composite phase change materials generated from cellulose presented a highly interesting choice for thermal management and renewable thermal energy storage.

Keywords cellulose, polyelectrolytes, phase change materials, thermal energy storage, light-to-thermal conversion

Received July 5, 2022; accepted November 5, 2022

E-mails: wangyg@nefu.edu.cn (Wang Y.), yxie@nefu.edu.cn (Xie Y.)

1 Introduction

Nowadays, it has been urgently challenged to solve the depletion of natural resources and find renewable, abundant, and environmentally friendly alternative energy forms [1]. Phase change materials (PCMs) are widely regarded as one of the most promising energy-saving materials at the moment owing to their outstanding advantages such as high latent heat storage density [2], almost constant use temperature [3], a wide temperature range for various applications [4], and a relatively low cost [5]. According to the type of phase change, PCMs can be divided into four classifications, including solid–solid, solid–liquid, solid–gas, and liquid–gas [6]. Hereinto, solid–liquid PCMs garner the most attention due to their remarkable superiority in terms of good thermal reliability, high latent heat storage capacity, low cost, and small volume change during the phase change process [7]. As a vital organic solid–liquid PCM, polyethylene glycol (PEG) is a non-toxic and non-corrosive polymer with good chemical stability, suitable phase change temperature, and high latent heat storage capacity [8,9]. However, PCMs have two major drawbacks that limit their applications: the first is their low thermal conductivity, which has a negative impact on energy conversion efficiency and decreases thermal charging and discharging; the second is PCM leakage during the phase transition [10].

Given that, considerable efforts have been devoted to addressing these technical issues. To resolve the drawback of low thermal conductivity, one effective strategy is to make composite PCMs with additives of high thermal conductivity additives, especially carbon-based additives with high thermal conductivity, stable thermal and chemical properties, low density and good

compatibility, to improve heat transfer rate and solar to thermal conversion capacity [11]. Composite PCMs can not only store and release energy through the phase transition process, but also effectively absorb solar energy and convert into thermal energy. Graphene oxide (GO) and carbon nanotube (CNT) are mostly used carbon-based additives. Advincula et al. [12] successfully encapsulated stearic acid into a shell composed only of reduced GO nanosheets. The carbon shell prevented leakage of stearic acid and significantly improved the thermal conductivity. Sun et al. [13] fabricated a novel phase change microcapsule system composed of an *n*-docosane core and a CNTs/polydopamine/silica hierarchical shell. The presence of CNTs/polydopamine coating layer could introduce an efficient solar light-to-heat energy conversion capability to the microcapsule system.

It is challenging to maintain PCMs in materials especially when undergoing a shift to liquid from solid phase. Thus, an effective strategy that closed containers serve as shape-stabilization supporting materials is proposed to prevent the leakage and improve the energy storage performance of PCMs [14]. According to the materials designs and dimensions, supporting materials applied to confine PCMs include core–shell, longitudinal, interfacial, and porous template structures [15]. Among these methods, the core–shell structure turns to be very promising to stabilize organic PCMs [16]. Compared to synthetic polymer-derived supporting materials, such as poly(methyl methacrylate) [17], poly(urea-urethane) [18], and polyimide [19], natural polymer-derived supporting materials, for example, cellulose, are more appealing in some cases thanks to their natural abundance, low cost, low toxicity, biocompatibility, and biodegradability [20]. Various cellulose-based supporting materials such as foams [2], aerogels [22], fibers [23] and capsules [24] have been widely used to stabilize PCMs. Yuan et al. [25] prepared core–shell microcapsules with ethyl cellulose and methylcellulose as the supporting material. The capsule shell can reduce the impact of the external environment on PCMs and prolonged their lifetime [26]. Besides, the encapsulation of PCMs produces more heat transfer area and thereby enhances the heat transfer rate [27]. Though cellulose-derived shape-stabilized PCMs have been studied to some extent, there still exists much research space regarding developing novel supporting structures and improving energy storage performance.

In this study, we prepared porous capsules with the representative core−shell structure. The capsules were formed via cooperative electrostatic interactions among cellulose-based polyelectrolyte complexes (CPEC), where cellulose 6-(*N*-pyridinium)hexanoyl ester (CPHE) that was synthesized in a one-pot reaction acted as the cationic polyelectrolyte, carboxymethyl cellulose (CMC) acted as the anionic polyelectrolyte, and cellulose nanofiber (CNF) enhanced the porous structure. After mixing CPHE, CMC, and CNF in a certain proportion and then freeze-drying, the porous CPEC capsules were formed. To improve thermal conductivity and light-to-thermal conversion efficiency, CNT and GO were incorporated into the porous CPEC capsules, respectively, which generated two composite porous capsules, namely, CPEC/CNT and CPEC/GO porous capsules. Furthermore, to form PEG-based composite PCMs, PEG was encapsulated into the prepared porous capsules, including CPEC, CPEC/CNT, and CPEC/GO, through the vacuum impregnation method. The resulted composite PCMs were referred to as PEG@CPEC, PEG@CPEC/CNT and PEG@CPEC/GO, respectively. The weight gained rate (WGR) values of PEG in these capsules were over 28 $g \cdot g^{-1}$. The obtained composite PCMs, especially PEG@CPEC/CNT and PEG@CPEC/GO, exhibited excellent shape stability, superior energy storage capacity and improved light-to-thermal conversion ability.

2 Experimental

2.1 Materials

Microcrystalline cellulose (MCC) was purchased from Sigma-Aldrich. CMC, 6-bromohexanoyl chloride, anhydrous pyridine, dimethyl sulfoxide, ferric chloride, PEG (M_n = 10000 $g \cdot mol^{-1}$) and CNT were obtained from Shanghai Aladdin Reagent Co. CNF was bought from Guilin Qihong Technology Co. GO was purchased from Shandong OBO New Material Co. Distilled water was used in all experiments. The other chemicals were all analytical grade and used as received.

2.2 Synthesis of CPHE

In a typical case, 0.5 g of MCC was dried in a vacuum oven at 90 °C for 24 h before it was suspended in 15 mL of pyridine. The cellulose suspension was heated up to the reaction temperature and followed by addition of certain amount of 6-bromohexanoyl. The resultant mixture was kept stirring for one hour. Then 5 mL of dimethyl sulfoxide was dropwise added into the system and the reaction was kept for a time. The resultant mixture was poured into 50 mL of distilled water and then transferred into a dialysis membrane (with a molecular weight cut-off of 8000) and stored in 4 L of water for 12 h. The water was changed ten times after every 12 h. After the dialysis process, the product was dissolved in water and stored for further use. The detailed reaction conditions were summarized in Table 1.

2.3 Preparation of CPEC, CPEC/GO and CPEC/CNT porous capsules

CPHE-3 was chosen as the polycation to construct porous

Table 1 Reaction conditions and results of CPHEs

Sample	Temperature/°C	Time/h[a)]	Molar ratio[b)]	N/(wt %)[c)]	*DS*	Solubility[d)]
CPHE-1	50	2	2	–	–	–
CPHE-2	100	2	1	3.27	0.94	–
CPHE-3	100	2	2	4.43	2.70	+
CPHE-4	100	5	2	4.49	2.91	+

a) The reaction time after adding dimethyl sulfoxide; b) the molar ratio of 6-bromohexanoyl to the hydroxyl group in cellulose; c) the content of N/(wt %) in CPHEs; d) the solubility of CPHEs in water ("–" represents insoluble in water, and "+" represents soluble in water).

capsules and referred to as CPHE. First, 200 mg of dried CMC and 100 mg of dried CNF were added into 10 mL of distilled water, respectively. The CMC/CNF mixture was continuously stirred for a few hours until CMC was completely dissolved and CNF was well dispersed in water. Then, GO and CNT in different contents (0.5, 1 and 3 wt %) were dispersed into the CMC/CNF mixture, respectively, via ultrasonication. The resultant sticky suspension was dropped into the CPHE aqueous solution (20 mg·mL^{-1}). Once the droplet was immersed into the CPHE solution, it would be solidified as a spheric capsule due to the formation of a polyelectrolyte complex network between CPHE acting as the polycation and CMC acting as the polyanion. After stabilization in the CPHE solution for five hours, the capsules were soaked in $FeCl_3$ solution (1 wt %) for one hour and subsequently rinsed with a large excess of distilled water. Finally, the capsules were freeze-dried to form dried porous capsules. Based on the content of GO or CNT, the obtained dried porous capsules were referred to as CPEC (without GO or CNT), CPEC/GO-0.5, CPEC/GO-1, CPEC/GO-3, CPEC/CNT-0.5, CPEC/CNT-1, CPEC/CNT-3.

2.4 Preparation of composite PCMs

The composite PCMs were prepared by encapsulating PEG into porous capsules through a vacuum impregnation method. Briefly, capsules including CPEC, CPEC/GO, and CPEC/CNT were immersed in melted PEG at 80 °C, respectively, and then placed in a vacuum drying oven (80 kPa) for 1.5 h. The excessive PEG was removed and the resultant shape-stable PCMs were cooled and stored for further use. The obtained composite PCMs were named as PEG@CPEC, PEG@CPEC/GO-0.5, PEG@CPEC/GO-1, PEG@CPEC/GO-3, PEG@CPEC/CNT-0.5, PEG@CPEC/CNT-1, PEG@CPEC/CNT-3. The *WGR* value of PEG in the capsules was calculated by Eq. (1):

$$WGR = \frac{m - m_0}{m_0}, \quad (1)$$

where m_0 and m were the initial mass of the capsules and the mass of the composite PCMs, respectively.

2.5 Thermal transport performance

The thermal transport performance of the composite PCMs was characterized using an infrared thermal imaging camera (Fotric 226s-L28, China). Samples on a glass were placed on a heating/cooling apparatus for heating to 100 °C (the set temperature) and cooling to 20 °C.

2.6 Light-to-thermal conversion test

A light-to-thermal conversion experiment of the composite PCMs was performed under simulated sunlight using a CEL-HXUV300 xenon lamp (CEAULIGHT, China). The intensity of irradiation was sustained at 300 mW·cm^{-2} while the irradiation distance was sustained constant at 10 cm from the light source. The temperature variations in the samples were recorded by the infrared thermal imaging camera.

2.7 Characterization

Liquid-state ^{1}H and ^{13}C nuclear magnetic resonance (NMR) spectra (AVANCE III HD 500 MHz, Bruker, Switzerland), Fourier transform infrared spectroscopy (FTIR, Nicolette 6700, Thermo Fisher Scientific, MA, USA) and X-ray photoelectron spectroscopy (XPS, ESCALAB, Thermo Fisher Scientific, MA, USA) were used to study the chemical structure of CPHEs. The element content of CPHEs was determined by elemental analysis (PE SERIES II 2400, PERKINELMER, MA, USA). The morphology of the sample was characterized by scanning electron microscope (SEM, Apreo S HiVac, Thermo Fisher Scientific, MA, USA). The phase change property was characterized using differential scanning calorimetry (DSC, TA Instruments, USA). The thermal conductivity of porous capsules was measured at 25 °C using a thermal conductivity tester (DRX-II-RL, China).

3 Results and discussion

3.1 Synthesis and characterization of CPHEs

In this study, the CPHEs as cationic pyridinium cellulose-based polyelectrolytes were synthesized via a facile one-pot method with the presence of MCC, 6-bromohexanoyl chloride and pyridine (Fig. 1(a)). In this system, the esterification was conducted between the hydroxyl group of MCC and the acyl chloride of 6-bromohexanoyl chloride, meanwhile the C–Br bond on the grafting agent was subjected to nucleophilic attack by pyridine to create the pyridinium ions [28]. A summary of the reaction conditions and results is given in Table 1. When the reaction temperature was 50 °C, the reaction was not completed. A large amount of unreacted cellulose remained in the system, but when the reaction temperature was raised, the cellulose was reacted and a clear, transparent solution was obtained (Fig. S1, cf. Electronic Supplementary Material,

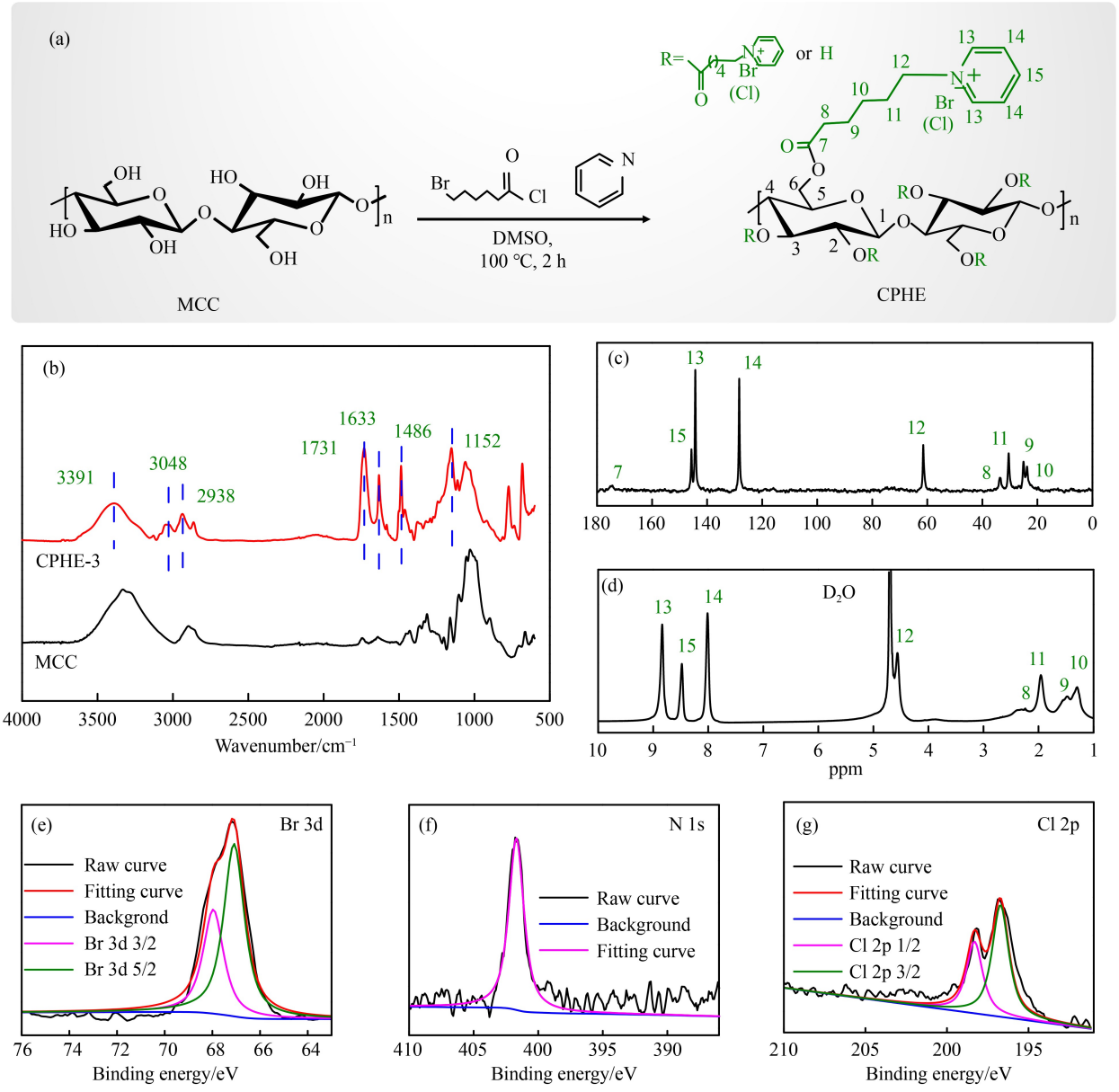

Fig. 1 (a) The synthesis route of CPHEs; (b) FTIR spectra of CPHE-3 and MCC; liquid-state (c) ^{13}C and (d) ^{1}H NMR spectra of CPHE-3; XPS spectra for CPHE-3: (e) Br 3d, (f) N 1s, and (g) Cl 2p.

ESM). The element nitrogen in CPHEs originated from pyridine, so its content was applied to represent the degree of substitution (*DS*) of CPHEs. The *DS* value of CPHEs were calculated based on the nitrogen content by Eq. (2) [29]:

$$DS = \frac{162 \times N\%}{14 - 256.1 \times N\%}, \quad (2)$$

where 162, 14, and 256.1 are the molar mass of the anhydroglucose unit, the element nitrogen, and the substituent quaternary ammonium group, respectively.

The *DS* value based on the nitrogen content of CPHEs varied as the reaction condition changed, such as the ratio of the esterification reagent to the hydroxyl group of cellulose, reaction temperature, and the reaction time. As shown in Table 1, the CPHE-3 and CPHE-4 had high *DS* of 2.70 and 2.91, respectively, which indicated that almost all the hydroxyl groups in cellulose were substituted leading to products of good aqueous solubility.

When comparing the FTIR spectra of MCC and CPHEs, there were plenty of new peaks within the spectrum (Figs. 1(b) and S2, cf. ESM). The peak at 1731 cm^{-1} was attributed to the C=O stretching vibration in carbonyl groups while the peak at 1633 cm^{-1} was due to the C=C vibration in the aromatic ring, which implies the pyridinium moieties were successful grafted [28]. In the case of CPHE-1 and CPHE-2, the lower signals at 1731 and 1633 cm^{-1} indicated that the damage of the intermolecular hydrogen bonding of the cellulose was not significant, which was therefore responsible for the basic

insolubility properties of the cellulose (Fig. S1). Contrarily, the higher intensity of the corresponding peaks in FTIR spectra for CPHE-3 and CPHE-4 indicated the obvious destruction of the intermolecular hydrogen bonding and sufficient esterification (Figs. 1(b) and S2). Thus, CPHE-3 and CPHE-4 were well solvable in water (Fig. S1). In addition, other characteristic signals of CPHEs were also be observed. A broad peak at 3391 cm^{-1} could be ascribed to the =C–H stretch vibration from pyridinium in *ortho*, *meta*, and *para* positions while the peaks at 1468 and 1152 cm^{-1} were assigned to the vibration of the C=N bond within the pyridinium ring and the stretching vibration of the C–N bond between the first carbon atom of the aliphatic chain and the nitrogen atom in the pyridinium ring, respectively [30]. The peaks at 3048 and 2938 cm^{-1} were the asymmetric and symmetric stretching of the C–H bond in aliphatic chains [31], respectively.

The NMR spectra of CPHEs showed the signals of cellulose backbone, 6-bromohexanoyl, and pyridinium groups (Figs. 1(c), 1(d) and S3, cf. ESM). Within the ^{13}C NMR spectra, the carbons in the C=O group produced the signal at 174.43 ppm. The signals at 145.90, 144.29, and 128.34 ppm were attributed to carbon atoms in the pyridinium ring. The signal at 61.47 ppm was derived from the carbon in the $C–N^+$ group. Also, signals between 40 and 20 ppm were owing to the carbon atoms in the saturated aliphatic chain of the 6-bromohexanoyl moiety [32]. Within the ^1H NMR spectra, the signals at 8.84, 8.48, and 8.01 ppm were ascribed to the protons in the pyridinium ring. The signal at 4.56 ppm originated from the proton on the methylene group attached to the $C–N^+$ group. Then, the signals ranged from 2.3 to 1.2 ppm were from the protons in the 6-bromohexanoyl moiety [33].

To further explore the existence forms of bromine and nitrogen in CPHEs, XPS was then used to get a detailed insight into CPHEs. In the XPS study CPHE-3, the spectra of Br 3d and N 1s photoelectron lines shown in Figs. 1(e) and 1(f) were representative for charged ions. The peak at 67.18 eV in Fig. 1(e) indicated bromine existed as the anionic bromine in the product. There were two types of Br photoelectrons, which were Br 3d 5/2 at 67.08 eV and Br 3d 3/2 at 67.98 eV, respectively. Furthermore, the absence of the peak regarding the C–Br bond at 70.4 eV in the spectrum indicated that bromine only existed as the anion [34]. The nitrogen signal in CPHEs could only originate from the pyridinium group. Indeed, the nitrogen 1s peaks with a binding energy of 401.58 eV (Fig. 1(f)) corresponded to a positively charged environment, namely, the pyridinium substituent. The absence of other nitrogen peak further showed that there was no remaining unreacted pyridine [35]. Besides, the Cl 2p spectrum (Fig. 1(g)) was also spotted through XPS. It was clear that there were two peaks (Cl 2p 3/2 at 196.78 eV and Cl 2p 1/2 at 198.28 eV, respectively) resulting from the chloride ion [36]. The chloride was from the acyl chloride moiety which underwent an esterification reaction and got attracted by pyridinium, thus remaining in CPHEs. The XPS analysis further proved that pyridinium cations were formed by nucleophilic attack on the C–Br bond.

3.2 Structure and morphology of CPEC-based porous capsules and the composite PCMs

CPHE-3 was chosen for the preparation of porous capsules and named CPHE in the following section. CPEC capsules were produced through ionically crosslinking interactions among CPHE and the CMC/CNF mixture (Scheme 1 and Fig. S4, cf. ESM). By dropping the CMC/CNF mixture into the CPHE solution, capsules were generated from the solvent immediately (Fig. S4(a)). However, after the freeze-drying process, the capsules were loose and hardly to form a solid shell for preparing the composite PCMs (Fig. S4(b)), because the electrostatic interaction was too weak to keep a stable network structure. Crosslinking was a crucial factor in inducing the molecular structural association to form a stable network, which could affect the properties of the final products, namely stability, porosity, and homogeneity of the capsules [37]. Thus, it was necessary to choose an

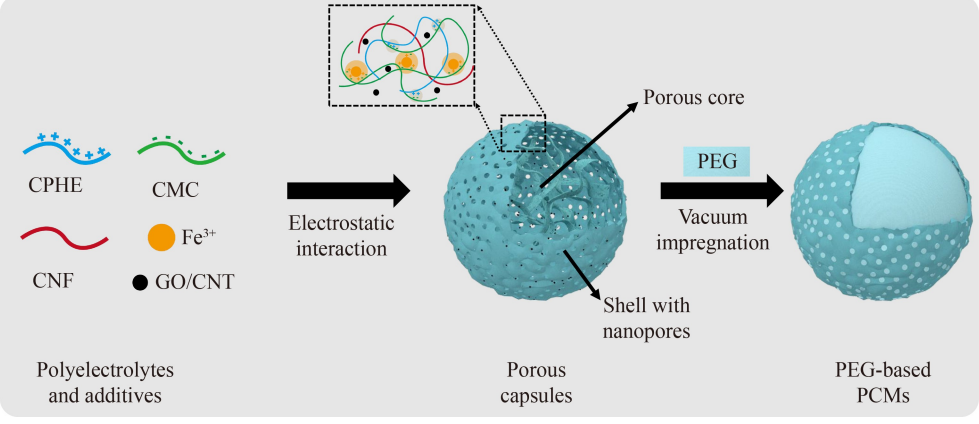

Scheme 1 Schematic illustration for the preparation of CPEC-based porous capsules and the PEG-based composite PCMs.

additional cross-linking agent to enhance the stability of the capsules. CMC was a natural polymer containing multiple carboxyl groups that exhibited an outstanding coordination ability with metal ions, such as ferric ion (Fe^{3+}) [38]. Thus, Fe^{3+} was added into the system (Scheme 1). It was obviously observed that the leakage of capsules disappeared with the addition of Fe^{3+} after freeze-drying (Figs. S4(c) and S4(d)) since metal ions distributed in the network improved the stability of capsules [39].

To further seek an efficient way to enhance the light-to-thermal conversion ability of CPEC-based capsules, GO and CNT were introduced to CPEC-based porous capsules to form CPEC/GO and CPEC/CNT capsules, respectively. The FTIR spectra of CPEC-based capsules in Fig. S5 (cf. ESM) showed a series of intensive absorption peaks at 1735 cm^{-1} for the C=O bond, 1634 cm^{-1} for the C=C bond, and 1151 cm^{-1} for the C–N bond. These absorption peaks of CPEC/GO and CPEC/CNT capsules were consistent with the characteristic absorption bands of CPEC capsules, which indicated that the introduction of GO or CNT did not affect the chemical structure of the formed capsules. The photo and SEM images of capsules obtained after freeze-drying were shown in Figs. 2, S6 and S7 (cf. ESM). Compared with CPEC capsule, CPEC/GO and CPEC/CNT capsules exhibited darker colors on account of the existence of GO and CNT, respectively (Figs. 2(a_1–c_1) and S7(a_1–d_1)). The porous structures were comprehensively further characterized with SEM. The addition of GO or CNT did not change the inherent structure of the capsule. Moreover, the resultant capsules showed a core–shell structure (Fig. S6). The acquired SEM images of the outer shell of the capsules displayed a dense structure with unevenly distributed nanopores (Figs. 2(a_2–c_2) and S7(a_2–d_2)). However, the internal structure of capsules was loosely constructed by a flaky or filamentous network structure (Figs. 2(a_3–c_3) and S7(a_3–d_3)) which could be explained by the electrostatic interactions mainly occurring at the surface of two polyelectrolyte solutions resulting in a relatively insoluble complex shell. The nanopores in the shell provided channels for subsequent PEG impregnation, and empty space within the porous core acted as a storage location for PEG.

To fabricate the PEG-impregnated composite PCMs, PEG was molten into a liquid at 80 °C and then filled into

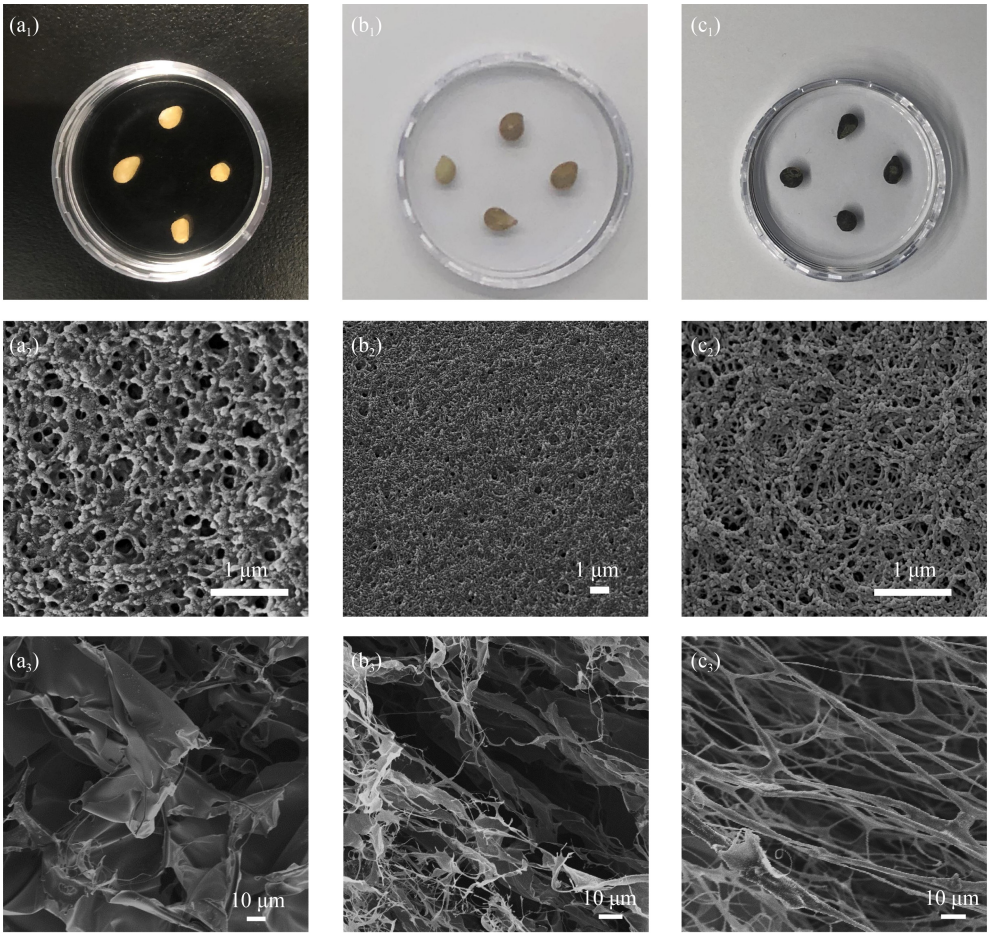

Fig. 2 Photos of (a_1) CPEC, (b_1) CPEC/GO-3, and (c_1) CPEC/CNT-3; SEM images of the surface structures for (a_2) CPEC, (b_2) CPEC/GO-3, and (c_2) CPEC/CNT-3; SEM images of the inner structures for (a_3) CPEC, (b_3) CPEC/GO-3, and (c_3) CPEC/CNT-3.

the capsules by the vacuum impregnation method (Scheme 1). The photo and SEM images of PCMs were shown in Figs. 3 and S8 (cf. ESM). As shown in Figs. 3(a_1–c_1) and S8(a_1–d_1), the shape of composite PCMs exhibited no obvious change after vacuum impregnation. All porous structures disappeared and only smooth areas could be observed for the capsules after impregnation of PEG (Figs. 3(a_2–c_2) and S8(a_2–d_2)), which indicated full encapsulation of PEG into the capsules resulted from the reinforced interaction of the van der Waals forces and hydrogen bonds [40] between hydrophilic PEG and the supporting matrix rich in hydrophilic hydroxyl groups, effectively limited PEG leakage during the phase change transition. The WGR study was revealed in Fig. 3(d). The weight for each composite PCM was hugely improved, and the WGR values for all the composite PCMs were more than 28 $g \cdot g^{-1}$. The addition of GO or CNT had no significant effect on the impregnation amount of PEG. The data of the PEG loading rate obtained from relevant references and our experiment were summarized in Table S1 (cf. ESM). It was clear that the porous capsule developed in our work exhibited a much better PEG loading rate than most conventional PEG-based PCMs in relevant references, which was due to the effective protection of the PEG core from leaking and flowing away in its molten state.

3.3 Thermal behavior of composite PCMs

The thermal energy storage capacity of the PCMs directly related to their phase transition temperature and latent heat density. The results about thermal behavior of composite PCMs were shown in (Fig. 4). The DSC curves of PEG and the composite PCMs were displayed in Fig. 4(a), and the corresponding thermal parameters including the melting temperature (T_m), the temperature of the crystallization (T_c), and the latent heat were summarized in Table 2. Notably, the DSC curves of the composite PCMs were similar to that of PEG indicating that the presence of the CPEC-based porous capsules did not alter the crystalline structure of PEG (Fig. 4(a)). As shown in Table 2, T_m and T_c of the composite PCMs slightly shifted towards the higher temperatures (around 65 and 42 °C), respectively, compared with those of PEG (T_m = 63.86 °C and T_c = 40.58 °C), which was due to the slightly restricted free movement of PEG chains in the porous network. In Table 2, the latent heat values of H_m and H_c for PEG were 144.4 and 141.8 $J \cdot g^{-1}$, respectively, while those for the composite PCMs in the melting and crystallization process were over 135.6 and 131.2 $J \cdot g^{-1}$, respectively, which were more than 93.9% and 92.5% of those regarding pure PEG, and thus showed excellent thermal energy storage capacity for the composite PCMs.

Furthermore, the enthalpy efficiency (λ) as an indispensable parameter was utilized to evaluate the energy storage property. The larger value of λ generally meant a better heat storage capacity [41]. The λ was calculated by Eq. (3)

$$\lambda = \frac{H_{m,PEG@CPEC}}{H_{m,PEG}} \times 100\%, \quad (3)$$

where $H_{m,PEG@CPEC}$ and $H_{m,PEG}$ represented the melting enthalpies of the composite PCMs and pure PEG, respectively. The λ values of all the composite PCMs were greater than 93 (Table 2), specifying that all the composite PCMs had excellent energy storage capacities.

The shape and thermal cycling stabilities of the composite PCMs were further evaluated. Samples of PEG and the composite PCMs were gradually heated on the heating apparatus plate from 20 (Fig. 4(b)) to 90 °C (Fig. 4(c)). The PEG gradually melted into a liquid state, but the composite PCMs kept their solid-state shapes from the beginning to the end without any leakage observed even at 90 °C for a few hours (Fig. 4(c)), which demonstrated that the composite PCMs possessed outstanding shape stabilities due to the introduction of capsules featured with a stable cross-linked porous network structure. The thermal cycling stability of PEG@CPEC, PEG@CPEC/GO-3, and PEG@CPEC/CNT-3 was further evaluated with 200 heating-cooling DSC cycles as shown in Figs. 4(d–f), with related data listed in Table S2 (cf. ESM). The curves after 200 heating-cooling cycles were almost

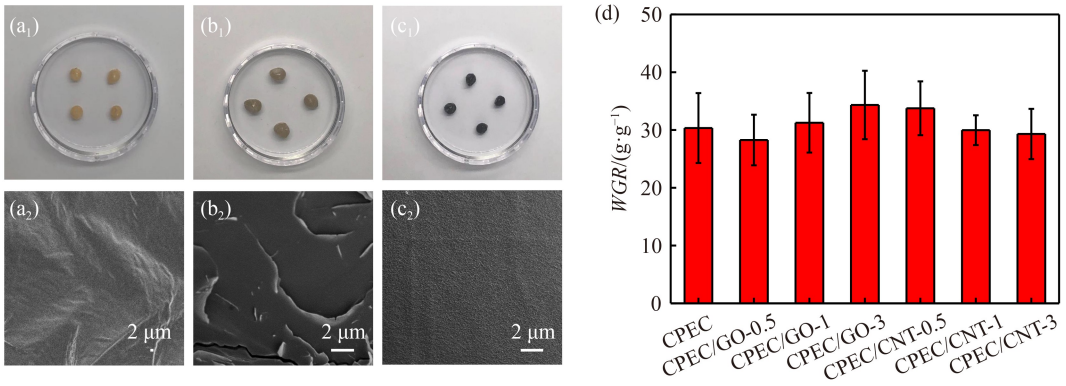

Fig. 3 Photos of (a_1) PEG@CPEC, (b_1) PEG@CPEC/GO-3, and (c_1) PEG@CPEC/CNT-3; SEM images of (a_2) PEG@CPEC, (b_2) PEG@CPEC/GO-3, and (c_2) PEG@CPEC/CNT-3; (d) the WGR values for the obtained PEG-based composite PCMs.

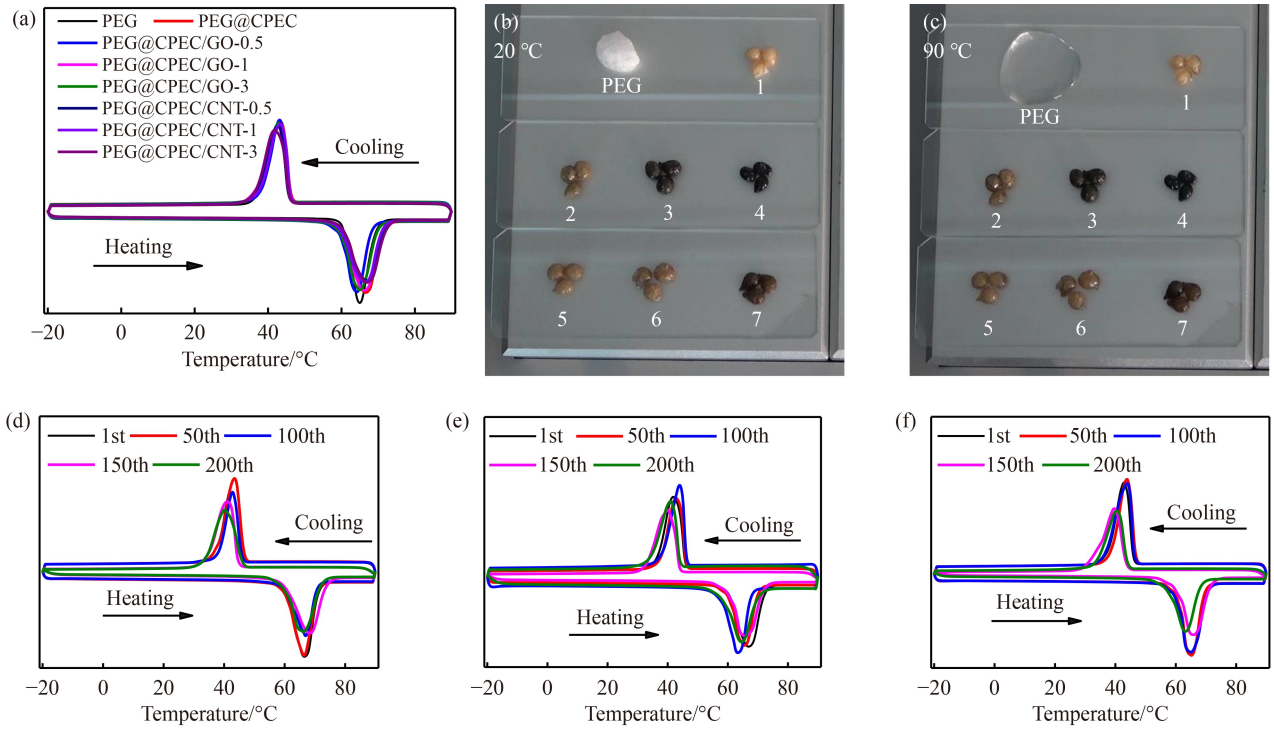

Fig. 4 (a) DSC curves of PEG and composite PCMs; leakage test photos of PEG and the composite PCMs at (b) 20 °C and (c) 90 °C (samples 1–7 represented the samples of PEG@CPEC, PEG@CPEC/CNT-0.5, 1, 3, PEG@CPEC/GO-0.5, 1, and 3, respectively); DSC curves of (d) PEG@CPEC, (e) PEG@CPEC/GO-3, and (f) PEG@CPEC/CNT-3 after the 1st, 50th, 100th, 150th, and 200th heating and cooling cycles.

Table 2 DSC results of PEG, PEG@CPEC, PEG@CPEC/GO and PEG@CPEC/CNT

Sample	Melting process		Crystallization process		λ
	T_m/°C	H_m/(J·g^{-1})	T_c/°C	H_c/(J·g^{-1})	
PEG	63.86	144.4	40.58	141.8	–
PEG@CPEC	65.41	139.5	42.51	136.9	96.6
PEG@CPEC/GO-0.5	65.01	140.6	42.23	138.2	97.4
PEG@CPEC/GO-1	64.72	142.0	42.12	135.0	98.3
PEG@CPEC/GO-3	65.47	142.2	42.32	137.4	98.5
PEG@CPEC/CNT-0.5	65.36	136.5	42.57	134.8	94.5
PEG@CPEC/CNT-1	65.59	135.6	41.83	136.1	93.9
PEG@CPEC/CNT-3	64.98	138.6	42.67	131.2	95.9

remained unchanged. The values of H_m and H_c for PEG@CPEC, PEG@CPEC/GO-3, and PEG@CPEC/CNT-3 were 129.9 and 124.4, 122.1 and 118.6, 119.1, and 107.2 J·g^{-1}, respectively (Table S2). During the heating–cooling cycles, melting and crystallization points did not exhibit a clear changing trend while melting and crystallization enthalpies showed a slightly decreasing trend which implied that the prepared composite PCMs showed excellent thermal stability.

3.4 Thermal transport and conversion of composite PCMs

Thermal transport and conversion were considered as important properties for PCM materials [42,43]. Thermal transport during the heating process and light-to-thermal energy conversion under light irradiation of the composite PCMs were evaluated (Figs. 5 and 6). Figures 5(a–b) showed the temperature development curves of PEG@CPEC/GO and PEG@CPEC/CNT with CPEC and PEG@CPEC as control samples during the heating and cooling processes. When the temperature was set to 90 °C and the heater was turned on, the sample temperatures increased from ca. 21 °C and remained constant over 65 °C. Comparing with CPEC, all composite PCMs showed a similar temperature changing trend, which displayed two thermal storage plateaus at around 60 °C during the heating process and around 50 °C during the cooling process. These temperature plateaus were due to the latent heat energy storage and the release of encapsulated PEG during the phase change process. Furthermore, the addition of GO or CNT to the prepared composite PCMs did not obviously enhance the thermal transport performance

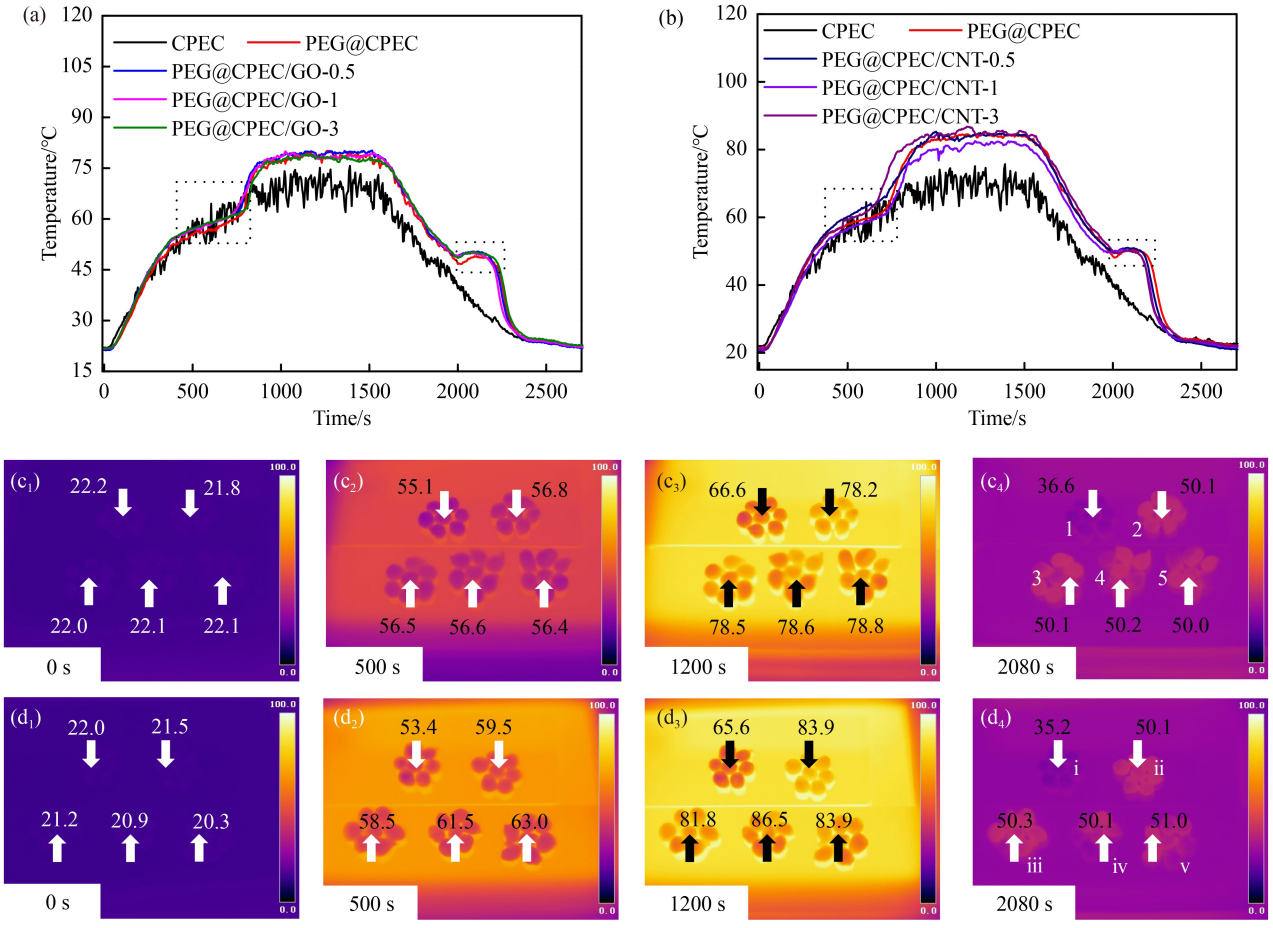

Fig. 5 The thermal transport performance of the samples: time-dependent temperature evolution curves of (a) PEG@CPEC/GO and (b) PEG@CPEC/CNT during heating and cooling (temperature plateaus during heating and cooling processes are correspondingly denoted by black rectangles); (c–d) infrared images showing temperature variations of samples during heating and cooling. Note: Samples 1, 2, 3, 4 and 5 in (c) represented CPEC, PEG@CPEC, PEG@CPEC/GO-0.5, PEG@CPEC/GO-3, and PEG@CPEC/GO-1, respectively. Samples i, ii, iii, iv and v in (d) represented CPEC, PEG@CPEC, PEG@CPEC/CNT-1, PEG@CPEC/CNT-3, and PEG@CPEC/CNT-0.5, respectively. The numbers above or below the arrows in (c) and (d) denoted the temperatures (°C) of the corresponding samples.

and the temperature development curves of PEG@CPEC/GO and PEG@CPEC/CNT showed a similar trend to that of PEG@CPEC. It could also be proved from the thermal conductivity of the porous capsule. Incorporating GO or CNT into the prepared capsules did not improve the thermal conductivity significantly (Table S3, cf. ESM). This could be ascribed to the failure to form a continuous thermal conduction network due to the low content of GO or CNT [44]. Moreover, the content of GO or CNT in the composite PCMs showed no obvious effect on the thermal transport performance during the heating and cooling processes. To intuitively and visually observe the change in the transient temperature on the plate during the heating and cooling processes, the thermal infrared images were recorded (Figs. 5(c–d)). It was remarkable that the temperatures of all composite PCMs including PEG@CPEC, PEG@CPEC/GO, and PEG@CPEC/CNT were obviously higher than that of CPEC. This is attributed to the efficient thermal conversion and preservation of PEG@CPEC, PEG@CPEC/GO, and PEG@CPEC/CNT that hampered the direct energy transport to the surrounding air and therefore led to temperature rise [45]. In contrast, only CPEC exhibited an unstable temperature changing curve and a relatively lower constant temperature throughout the heating process resulting from the quick energy transmission to the environment (Figs. 5(a–b)). During the cooling process, the temperatures of PEG@CPEC, PEG@CPEC/GO, and PEG@CPEC/CNT were up by 13, 13, and 15 °C, respectively, higher than that of the CPEC at the cooling thermal storage plateau area (Figs. 5(c_4) and 5(d_4)). In addition, PEG@CPEC/CNT exhibited a slightly higher temperature in comparison with PEG@CPEC/GO during the heating process because the tube-like structure of CNT greatly facilitated the thermal conductivity along the axial direction of PEG@PEG/CNT [46].

Moreover, the light-to-thermal energy conversion capability of the composite PCMs was investigated under a simulated sunlight irradiation with a power density of 300 mW·cm^{-2} (Fig. 6). Upon light irradiation, GO and

CNT effectively converted the solar energy to the thermal energy and raised the temperatures of the PEG@CPEC/GO and PEG@CPEC/CNT. As shown in Fig. 6(a), compared with PEG@CPEC slow increasing to around 48.6 °C, irradiated PEG@CPEC/GO-0.5, PEG@CPEC/GO-1, and PEG@CPEC/GO-3 exhibited relatively sharp and sudden increases to temperatures at 59.5, 63.2, and 81.1 °C, respectively. Figure 6(b) also showed that PEG@CPEC/CNT-0.5, PEG@CPEC/CNT-1, and PEG@CPEC/CNT-3 exhibited a faster temperature increase to temperatures at 54.4, 71.7, and 98.6 °C, respectively, which was higher than that for PEG@CPEC. This indicated that the incorporation of GO or CNT into the composite PCMs effectively improved the light-to-thermal conversion capacity. In essence, the temperatures for PEG@CPEC/GO-3 and PEG@CPEC/CNT-3 were increased by 32.5 and 51.9 °C, respectively, in comparison with that for PEG@CPEC. The multi-walled structure of CNT provided a larger surface area for the incident light than GO, which caused PEG@CPEC/CNT-3 to absorb more light and conduct the heat to surrounding PEG faster compared to PEG@CPEC/GO-3 [47]. Thus, PEG@CPEC/CNT showed a higher temperature than that of PEG@CPEC/GO during the simulated sunlight irradiation. With light removed, temperatures of all samples dropped sharply. Subsequently, when the temperatures were near the crystallization point, the plateaus appeared obviously for PEG@CPEC/GO-1, PEG@CPEC/GO-3, PEG@CPEC/CNT-1, and PEG@CPEC/CNT-3, which showed that the corresponding PCMs gradually released the energy stored in the heating stage with plateaus for about 30, 180, 55, and 65 s, respectively (Figs. 6(c–d)). Thus, the PEG@

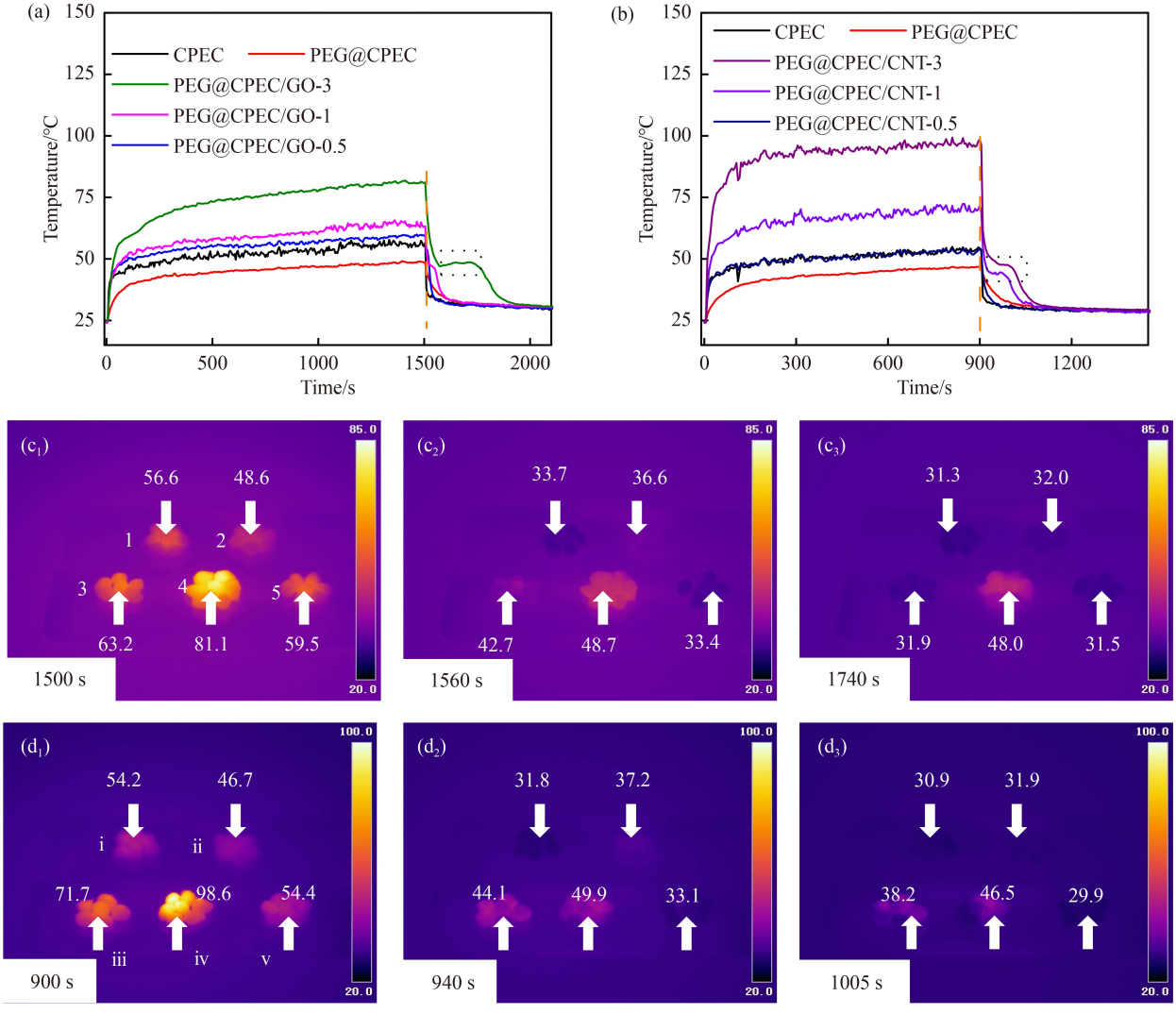

Fig. 6 The light-to-thermal conversion of samples: light-to-thermal conversion curves of (a) PEG@CPEC/GO and (b) PEG@CPEC/CNT (the black rectangles showed the temperature plateaus during the heating and cooling processes); (c–d) infrared images showing the temperature variations of samples during the cooling process. Note: samples 1, 2, 3, 4, and 5 in (c) represented the samples of CPEC, PEG@CPEC, PEG@CPEC/GO-1, PEG@CPEC/GO-3, and PEG@CPEC/GO-0.5, respectively. Samples i, ii, iii, iv, and v in (d) represented the samples of CPEC, PEG@CPEC, PEG@CPEC/CNT-1, PEG@CPEC/CNT-3, and PEG@CPEC/CNT-0.5, respectively. The numbers above or below the arrows in(c–d) denoted the temperatures (°C) of the corresponding samples.

CPEC/GO and PEG@CPEC/CNT composite PCMs, particularly PEG@CPEC/GO-3 and PEG@CPEC/CNT-3, significantly postponed the temperature decline during the cooling process which exhibited a promising application as temperature-controllable thermal management materials [48–50]. Comparably, the curves for PEG@CPEC, PEG@CPEC/GO-0.5 and PEG@CPEC/CNT-0.5 lacked platforms because their light absorption capacities were inadequate to reach the phase-transition temperatures and trigger the phase transition.

4 Conclusions

In this work, we prepared a new energy storage form-stable composite PCMs by taking CPEC capsules with GO or CNT as supports and PEG as the PCM, respectively. The CPEC capsules were constructed through cooperative electrostatic interactions among polyelectrolytes, which composed of the synthesized CPHE with the pyridinium group as the cationic polyelectrolyte, the CMC with the carboxyl group as the anionic polyelectrolyte, and CNF that enhanced the porous structure of the capsules. The prepared capsules presented a typical core–shell structure, with an excellent PEG loading capacity. The PEG loading efficiency of the composite PCMs reached more than 28 $g \cdot g^{-1}$. The resultant composite PCMs including PEG@CPEC, PEG@CPEC/GO, and PEG@CPEC/CNT displayed stabilized shape even at 90 °C because the porous network had strong hydrogen bonding interactions with PEG molecules and restricted molecular movement at high temperatures. The composite PCMs showed outstanding thermal energy storage capacities with their maximum latent heat values in the melting and crystallization processes reaching up to 142.2 and 138.2 $J \cdot g^{-1}$, respectively. The thermal cycling evaluations revealed that the composite PCMs possessed excellent thermal reliability. There was no obvious fatigue change in the DSC curves or the latent heat values after 200 times of thermal cycling. Moreover, incorporating GO or CNT into the composite PCMs dramatically enhanced the light-to-thermal conversion capability. Therefore, the PEG-based composite PCMs featured with multiple functions including high thermal energy storage capacity, remarkable thermal stability, and efficient light-to-thermal conversion performance showed a great potential in the field of renewable thermal energy storage and rendered a new avenue in high-efficiency solar thermal applications.

Acknowledgements This work was supported by the National Natural Science Foundation of China (Grant Nos. 31890774 and 31890770), the Fundamental Research Funds for the Central Universities (Grant No. 2572018AB40), and the National Training Program of Innovation and Entrepreneurship for Undergraduates of Northeast Forestry University (Grant No. 202110225432).

Electronic Supplementary Material Supplementary material is available in the online version of this article at https://dx.doi.org/10.1007/s11705-022-2279-3 and is accessible for authorized users.

References

1. Guo J, Jiang Y, Wang Y, Zou B. Thermal storage and thermal management properties of a novel ventilated mortar block integrated with phase change material for floor heating: an experimental study. Energy Conversion and Management, 2020, 205: 112288
2. Yang H, Bai Y, Ge C, He L, Liang W, Zhang X. Polyethylene glycol-based phase change materials with high photothermal conversion efficiency and shape stability in an aqueous environment for solar water heater. Composites Part A: Applied Science and Manufacturing, 2022, 154: 106778
3. Li C, Yu H, Song Y, Liu Z. Novel hybrid microencapsulated phase change materials incorporated wallboard for year-long year energy storage in buildings. Energy Conversion and Management, 2019, 183: 791–802
4. Huang Z, Gao X, Xu T, Fang Y, Zhang Z. Thermal property measurement and heat storage analysis of $LiNO_3$/KCl-expanded graphite composite phase change material. Applied Energy, 2014, 115: 265–271
5. Khan Z, Khan Z, Ghafoor A. A review of performance enhancement of PCM based latent heat storage system within the context of materials, thermal stability and compatibility. Energy Conversion and Management, 2016, 115: 132–158
6. Kee S Y, Munusamy Y, Ong K S. Review of solar water heaters incorporating solid-liquid organic phase change materials as thermal storage. Applied Thermal Engineering, 2018, 131: 455–471
7. Sun K, Kou Y, Zhang Y, Liu T, Shi Q. Photo-triggered hierarchical porous carbon-based composite phase-change materials with superior thermal energy conversion capacity. ACS Sustainable Chemistry & Engineering, 2020, 8(8): 3445–3453
8. Sun Z, Sun K, Zhang H, Liu H, Wu D, Wang X. Development of poly(ethylene glycol)/silica phase-change microcapsules with well-defined core–shell structure for reliable and durable heat energy storage. Solar Energy Materials and Solar Cells, 2021, 225: 111069
9. Zheng Z, Shi T, Liu H, Wu D, Wang X. Polyimide/phosphorene hybrid aerogel-based composite phase change materials for high-efficient solar energy capture and photothermal conversion. Applied Thermal Engineering, 2022, 207: 118173
10. Lang Z, Ju Y, Wang Y, Xiao Z, Wang H, Liang D, Li J, Xie Y. Cellulose-derived solid-solid phase change thermal energy storage membrane with switchable optical transparency. Chemical Engineering Journal, 2022, 435: 134851
11. Yu Z, Feng D, Feng Y, Zhang X. Thermal conductivity and energy storage capacity enhancement and bottleneck of shape-stabilized phase change composites with graphene foam and carbon nanotubes. Composites Part A: Applied Science and Manufacturing, 2022, 152: 106703
12. Advincula P A, de Leon A C, Rodier B J, Kwon J, Advincula R

C, Pentzer E B. Accommodating volume change and imparting thermal conductivity by encapsulation of phase change materials in carbon nanoparticles. Journal of Materials Chemistry A: Materials for Energy and Sustainability, 2018, 6(6): 2461–2467
13. Sun Z, Shi T, Wang Y, Li J, Liu H, Wang X. Hierarchical microencapsulation of phase change material with carbon-nanotubes/polydopamine/silica shell for synergistic enhancement of solar photothermal conversion and storage. Solar Energy Materials and Solar Cells, 2022, 236: 111539
14. Zhang L, An L, Wang Y, Lee A, Schuman Y, Ural A, Fleischer A S, Feng G. Thermal enhancement and shape stabilization of a phase-change energy-storage material via copper nanowire aerogel. Chemical Engineering Journal, 2019, 373: 857–869
15. Arshad A, Jabbal M, Yan Y, Darkwa J. The micro-/nano-PCMs for thermal energy storage systems: a state of art review. International Journal of Energy Research, 2019, 43(11): 5572–5620
16. Bahsi Kaya G, Kim Y, Callahan K, Kundu S. Microencapsulated phase change material via Pickering emulsion stabilized by cellulose nanofibrils for thermal energy storage. Carbohydrate Polymers, 2022, 276: 118745
17. Wang F, Zhang Y, Li X, Wang B, Feng X, Xu H, Mao Z, Sui X. Cellulose nanocrystals-composited poly (methyl methacrylate) encapsulated *n*-eicosane via a Pickering emulsion-templating approach for energy storage. Carbohydrate Polymers, 2020, 234: 115934
18. Yoo Y, Martinez C, Youngblood J P. Synthesis and characterization of microencapsulated phase change materials with poly(urea-urethane) shells containing cellulose nanocrystals. ACS Applied Materials & Interfaces, 2017, 9(37): 31763–31776
19. Zheng Z, Liu H, Wu D, Wang X. Polyimide/MXene hybrid aerogel-based phase-change composites for solar-driven seawater desalination. Chemical Engineering Journal, 2022, 440: 135862
20. Xu T, Liu K, Sheng N, Zhang M, Liu W, Liu H, Dai L, Zhang X, Si C, Du H, Zhang K. Biopolymer-based hydrogel electrolytes for advanced energy storage/conversion devices: properties, applications, and perspectives. Energy Storage Materials, 2022, 48: 244–262
21. Liu H, Du H, Zheng T, Liu K, Ji X, Xu T, Zhang X, Si C. Cellulose based composite foams and aerogels for advanced energy storage devices. Chemical Engineering Journal, 2021, 426: 130817
22. Cheng M, Hu J, Xia J, Liu Q, Wei T, Ling Y, Li W, Liu B. One-step *in-situ* green synthesis of cellulose nanocrystal aerogel based shape stable phase change material. Chemical Engineering Journal, 2022, 431: 133935
23. Qian Y, Han N, Gao X, Gao X, Li W, Zhang X. Cellulose-based phase change fibres for thermal energy storage and management applications. Chemical Engineering Journal, 2021, 412: 128596
24. Xiao D, Liang W, Xie Z, Cheng J, Du Y, Zhao J. A temperature-responsive release cellulose-based microcapsule loaded with chlorpyrifos for sustainable pest control. Journal of Hazardous Materials, 2021, 403: 123654
25. Yuan K, Liu J, Fang X, Zhang Z. Novel facile self-assembly approach to construct graphene oxide-decorated phase-change microcapsules with enhanced photo-to-thermal conversion performance. Journal of Materials Chemistry A: Materials for Energy and Sustainability, 2018, 6(10): 4535–4543
26. Lin Y, Zhu C, Alva G, Fang G. Microencapsulation and thermal properties of myristic acid with ethyl cellulose shell for thermal energy storage. Applied Energy, 2018, 231: 494–501
27. Han S, Lyu S, Wang S, Fu F. High-intensity ultrasound assisted manufacturing of melamine-urea-formaldehyde/paraffin nanocapsules. Colloids and Surfaces A: Physicochemical and Engineering Aspects, 2019, 568: 75–83
28. Jasmani L, Eyley S, Wallbridge R, Thielemans W. A facile one-pot route to cationic cellulose nanocrystals. Nanoscale, 2013, 5(21): 10207–10211
29. Pedrosa J F S, Rasteiro M G, Neto C P, Ferreira P J T. Effect of cationization pretreatment on the properties of cationic Eucalyptus micro/nanofibrillated cellulose. International Journal of Biological Macromolecules, 2022, 201: 468–479
30. Matandabuzo M, Ajibade P A. Synthesis, characterization, and physicochemical properties of hydrophobic pyridinium-based ionic liquids with *N*-propyl and *N*-isopropyl. Zeitschrift für Anorganische und Allgemeine Chemie, 2018, 644(10): 489–495
31. Tan W, Li Q, Dong F, Zhang J, Luan F, Wei L, Chen Y, Guo Z. Novel cationic chitosan derivative bearing 1,2,3-triazolium and pyridinium: synthesis, characterization, and antifungal property. Carbohydrate Polymers, 2018, 182: 180–187
32. Liu S, Edgar K J. Water-soluble co-polyelectrolytes by selective modification of cellulose esters. Carbohydrate Polymers, 2017, 162: 1–9
33. Rashid T, Kait C F, Regupathi I, Murugesan T. Dissolution of kraft lignin using protic ionic liquids and characterization. Industrial Crops and Products, 2016, 84: 284–293
34. Zhang X, Shen B, Zhu S, Xu H, Tian L. UiO-66 and its Br-modified derivates for elemental mercury removal. Journal of Hazardous Materials, 2016, 320: 556–563
35. Mao H, Fu Y, Yang H, Zhang S, Liu J, Wu S, Wu Q, Ma T, Song X M. Structure-activity relationship toward electrocatalytic nitrogen reduction of MoS_2 growing on polypyrrole/graphene oxide affected by pyridinium-type ionic liquids. Chemical Engineering Journal, 2021, 425: 131769
36. Shimizu K, Shchukarev A, Kozin P A, Boily J F. X-ray photoelectron spectroscopy of fast-frozen hematite colloids in aqueous solutions. 5. Halide ion (F^-, Cl^-, Br^-, I^-) adsorption. Langmuir, 2013, 29(8): 2623–2630
37. Shi W, Ching Y C, Chuah C H. Preparation of aerogel beads and microspheres based on chitosan and cellulose for drug delivery: a review. International Journal of Biological Macromolecules, 2021, 170: 751–767
38. Rasoulzadeh M, Namazi H. Carboxymethyl cellulose/graphene oxide bio-nanocomposite hydrogel beads as anticancer drug carrier agent. Carbohydrate Polymers, 2017, 168: 320–326
39. Yadollahi M, Farhoudian S, Barkhordari S, Gholamali I, Farhadnejad H, Motasadizadeh H. Facile synthesis of chitosan/ZnO bio-nanocomposite hydrogel beads as drug delivery systems. International Journal of Biological Macromolecules, 2016, 82: 273–278
40. Li Y, Sun K, Kou Y, Liu H, Wang L, Yin N, Dong H, Shi Q. One-step synthesis of graphene-based composite phase change

materials with high solar-thermal conversion efficiency. Chemical Engineering Journal, 2022, 429: 132439

41. Fang Y, Liu S, Li X, Hu X, Wu H, Lu X, Qu J. Biomass porous potatoes/MXene encapsulated PEG-based PCMs with improved photo-to-thermal conversion capability. Solar Energy Materials and Solar Cells, 2022, 237: 111559
42. Chen X, Cheng P, Tang Z, Xu X, Gao H, Wang G. Carbon-based composite phase change materials for thermal energy storage, transfer, and conversion. Advanced Science, 2021, 8(9): 2001274
43. Xue F, Lu Y, Qi X D, Yang J H, Wang Y. Melamine foam-templated graphene nanoplatelet framework toward phase change materials with multiple energy conversion abilities. Chemical Engineering Journal, 2019, 365: 20–29
44. Liu Y, Yang Y, Li S. Graphene oxide modified hydrate salt hydrogels: form-stable phase change materials for smart thermal management. Journal of Materials Chemistry A: Materials for Energy and Sustainability, 2016, 4(46): 18134–18143
45. Wang Y, Qiu Z, Lang Z, Xie Y, Xiao Z, Wang H, Liang D, Li J, Zhang K. Multifunctional reversible self-assembled structures of cellulose-derived phase-change nanocrystals. Advanced Materials, 2021, 33(3): e2005263
46. Hou S, Wang M, Guo S, Su M. Photothermally driven refreshable microactuators based on graphene oxide doped paraffin. ACS Applied Materials & Interfaces, 2017, 9(31): 26476–26482
47. Nandihalli N, Liu C J, Mori T. Polymer based thermoelectric nanocomposite materials and devices: fabrication and characteristics. Nano Energy, 2020, 78: 105186
48. Xie Y, Li W, Huang H, Dong D, Zhang X, Zhang L, Chen Y, Sheng X, Lu X. Bio-based radish@PDA/PEG sandwich composite with high efficiency solar thermal energy storage. ACS Sustainable Chemistry & Engineering, 2020, 8(22): 8448–8457